THE JOURNAL OF PHYSICAL CHEMISTRY A

ARTICLE

pubs.acs.org/JPCA

Modeling Energy Landscapes of Proton Motion in Nonaqueous, Tethered Proton Wires

Usha Viswanathan,[†] Dipankar Basak,[†] Dhandapani Venkataraman,[†] Justin T. Fermann,[†] and Scott M. Auerbach*[,†,‡]

[†]Department of Chemistry and [‡]Department of Chemical Engineering, University of Massachusetts Amherst, Amherst, Massachusetts 01003, United States

Supporting Information

ABSTRACT: We have modeled structures and energetics of anhydrous proton-conducting wires: tethered hydrogen-bonded chains of the form ···HX···HX···HX···, with functional groups HX = imidazole, triazole, and formamidine; formic, sulfonic, and phosphonic acids. We have applied density functional theory (DFT) to model proton wires up to 19 units long, where each proton carrier is linked to an effective backbone to mimic polymer tethering. This approach allows the direct calculation of hydrogen bond strengths. The proton wires were found to be stabilized by strong hydrogen bonds (up to 50 kJ/mol) whose strength correlates with the proton affinity of HX [related to pK_b(HX)] and not to pK_a(HX) as is often assumed. Geometry optimizations and ab initio molecular dynamics near 400 K on imidazole-based proton wires both predict that adding a proton to the end of such wires causes the excess charge to embed into the interior segments of these wires. Proton translocation energy landscapes for imidazole-based wires are sensitive to the imidazole attachment point (head or feet) and to wire architecture (linear or interdigitated). Linear imidazole wires with head-attachment exhibit low barriers for intrawire proton motion, rivaling proton diffusion in liquid imidazole. Excess charge relaxation from the edge of wires is found to be dominated by long-range Grotthuss shuttling for distances as long as 42 Å, especially for interdigitated wires. For imidazole, we predict that proton translocation is controlled by the energetics of desorption from the proton wire, even for relatively long wires (600 imidazole units). Proton desorption energies show no correlation with functional group properties, suggesting that proton desorption is a collective process in proton wires.

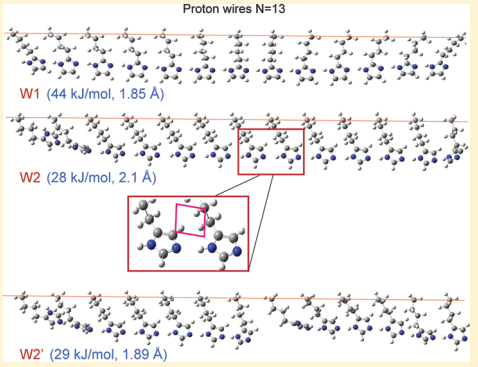

I. INTRODUCTION

Proton shuttling through hydrogen-bonded networks is a ubiquitous dynamical motif for energy and signal transduction in aqueous[1−21] and nonaqueous[22−31] systems. Such networks, hereafter denoted "proton wires", are composed of amphiprotic species such as water or imidazole—those that both donate and accept hydrogen bonds. Although several molecular modeling studies have shed light on proton transport in bulk[1,2] and confined water,[8−12] very little is known about the fundamentals of proton conduction in nonaqueous systems.[25,32−34] For example, polymers containing imidazole[35,36] and triazole[37−40] have received significant attention as replacements for hydrated Nafion in fuel cells,[35,36,40] based on the assumption that concerted (Grotthuss[41,42]) proton shuttling over long lengths will produce high proton conductivities in such materials. These studies are far from finding polymers with acceptable performance, due in part to incomplete understanding of how proton wire structure and functional group properties[40,43] relate to proton conductivity. In this article, we report density functional theory (DFT) modeling of nonaqueous, tethered proton wires, leading to new design criteria for optimizing long-range motion in proton conductors.

In solid-state conduction, unidirectional proton transport involves two distinct processes: proton shuttling followed by functional group rotation (proton wire regeneration) to allow subsequent proton translocation. Optimizing the composite process relies on a balance between alignment and flexibility of hydrogen bonds—a balance that has proven difficult to design a priori. For example, a conventional assumption when choosing functional groups is that ease of proton shuttling correlates with the pK_a of a proton-carrying group.[43,44] Although this may be reasonable for hydrated conductors such as Nafion, applying this notion to nonaqueous conductors rests on the questionable notion that protonating water resembles the concerted dynamics of shuttling along a proton wire. Not only does this assume a correlation between thermodynamics and kinetics of substantially different processes but also it ignores the importance of proton wire architecture which controls proton jump distances and hence barriers. In the present study, we apply DFT to compute energetics of proton wires with various functional

Received: June 4, 2010
Revised: April 26, 2011
Published: May 09, 2011

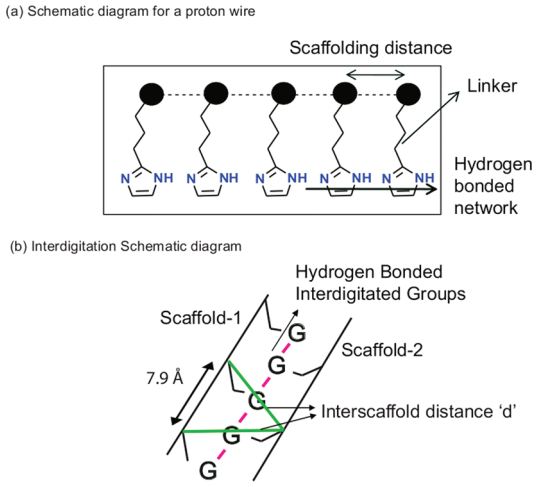

Figure 1. (a) Schematic diagram of a linear proton wire involving a rigid polymer backbone, linkers, and hydrogen-bonded amphiprotic groups (in this case imidazoles). (b) Schematic of interdigitation of functional groups from two rigid scaffolds to form proton wires W4, W5, and W6.

groups, using effective backbones to model polymer tethering. This allows a direct connection between wire stability and hydrogen bond energy; obtaining such a connection is otherwise quite challenging. Below we find that hydrogen bond energies correlate with functional group proton affinity [related to pK_b(HX)] and not with pK_a(HX) as is often assumed. Such a correlation for *tethered* hydrogen bond networks, which complements knowledge of $[A\cdots H{-}A]^{+}$[45] and $[A\cdots H{-}B]^{+}$ species,[46−51] may prove useful for designing proton conductors that balance rapid proton shuttling with efficient functional group regeneration.

Efficient proton conduction also requires clever design of proton wire architectures. Indeed, given the importance of functional group flexibility, it is not obvious that long-range Grotthuss shuttling is possible for tethered proton wires because tethering may impose conformational restrictions on functional groups that preclude low-barrier or barrierless concerted motions. This issue was studied by Cavalcanti et al. using classical simulations for imidazoles tethered to MCM-41 mesoporous silica,[32] but to date architecture effects have not been studied using quantum chemical methods. We investigate the balance between alignment and flexibility in the present study by considering proton wires with functional groups connected to effective polymer backbones by flexible linkers (Figure 1a). An important goal of this study is thus to predict backbone and linker design criteria that produce low-barrier proton motion. We also investigate the equilibrium distribution of excess charge in these wires, finding at both 0 and 400 K that a single excess charge embeds into interior segments of the wires. Finally, we explore the role of supramolecular architectures involving interdigitated proton wires, offering a facile mechanism for interwire proton motion. The calculations described below predict long-range Grotthuss shuttling in nonaqueous proton wires, especially for interdigitated architectures, for distances as long as 42 Å.

The remainder of this article is organized as follows: in Section II we describe the computational methods used to model the various proton wires; in Section III we discuss our predictions of proton wire structure, stability, and translocation dynamics; and in Section IV we offer concluding remarks.

II. METHODS

A. Unprotonated Wires. Several proton wires were modeled, each with a single type of proton-carrying moiety attached to a flexible alkyl linker. The terminal carbons of all linkers were constrained to lie on a line, mimicking attachment to bonding sites on a polymer backbone, as shown in Figure 1a with imidazole for example. This effective backbone approach allows a direct connection between wire stability and hydrogen bond energy by comparing energies of proton wires and monomer units (vide infra). In contrast, such a comparison with explicit, flexible backbones yields a mixture of hydrogen bond energy, backbone bond energy, and backbone distortion energy. As an added benefit of our present effective backbone treatment, we can study relatively long wires, up to 19 units long in the calculations reported below. Despite the simplicity and benefits of this approach, it has been established that backbone flexibility does play a role in proton transport, through the dependence of conductivities on polymer glass-transition temperatures.[52] To shed light on this, we will report in future work on a hierarchy of flexible models of effective and explicit backbones. The results of flexible backbone models can reference back to the present work to determine the role of backbone flexibility in proton conduction. We nonetheless expect that our present findings regarding functional group correlations and supramolecular wire architectures will remain qualitatively valid because our models build in flexibility through alkyl linkers as we discuss now.

For each wire type, we varied linker length (ethyl to pentyl) and backbone attachment distance (4.0−7.9 Å) to determine optimal configurations for wires of various lengths in the range 3−19 monomer units. The optimal linker length was defined as giving a proton affinity for the tethered wire equal to that of the corresponding unconstrained system, indicating sufficient flexibility to accommodate the added proton. Propyl linkers were generally found to satisfy this criterion.[32] Optimal backbone distances were identified as allowing continuous hydrogen bonding for the longest wires considered. These backbone distances were found to depend on the effective size of a proton-carrying functional group.

We built proton wires with functional groups HX = imidazole, triazole, formamidine, formic, sulfonic, and phosphonic acids, sampling groups with a range of proton affinities. We modeled the structures and energetics of both unprotonated and protonated systems, to determine wire stabilities, proton affinities, and energy landscapes of proton motion through these wires. For unprotonated wires, we performed geometry optimizations to compute how cohesive energies and hence hydrogen-bond strengths vary with functional group. For each protonated wire, we identified various local minima (including the overall ground state) for proton locations along the wire. For selected systems, we also computed transition states connecting local minima.

We also studied "interdigitated" wire assemblies involving hydrogen-bond networks with alternating groups linked to two parallel linear backbones. These are interesting for two reasons: they allow a study of interchain proton transport, likely important for macroscopic conduction, and they may allow proton wire formation from backbones with nonoptimal (too long) repeat lengths. Inspired by the polythiophene backbone being studied in our synthetic laboratory, we constructed interdigitated proton wires from two parallel backbones each with a repeat length of 7.9 Å and with an offset so that three adjacent functional groups are anchored to backbone points on an isosceles triangle as

shown in Figure 1b. We investigated both linear and interdigitated versions of imidazole- and triazole-based proton wires.

The various proton wires are henceforth denoted as follows:

- C = formic acid
- S = sulfonic acid
- P = phosphonic acid
- N = formamidine
- W1 or Im = linear wire with imidazole attached at the head carbon (Figure 1a)
- W2 = linear wire with imidazole attached at a foot carbon (Figure 4)
- W3 or Tr = linear wire with 1,2,3-triazole (Figure 9c)
- W4 = interdigitated version of W1
- W5 = interdigitated version of W2
- W6 = interdigitated version of W3

Proton wire stabilities for unprotonated systems were quantified by computing the n-mer-normalized cohesive energy, $E_{coh}(n)$, defined as

$$E_{coh}(n) \equiv \frac{|E_n - nE_1|}{n} \quad (1)$$

where E_1 and E_n are the optimized energies of a monomer and an n-mer, respectively, using the model chemistry described below. Such optimizations involve all atoms except for terminal carbons on linkers, henceforth denoted as "tethered" optimizations. Because we find only small conformational changes between free and tethered, hydrogen-bonded functional groups, we may safely assume that hydrogen bonding is predominantly responsible for the computed cohesive energies. As such, hydrogen bond strengths are given by $|(E_n - nE_1)|/m$, where m is the number of hydrogen bonds in a wire. These are easily identified as NH or OH intermolecular distances less than 2.5 Å. P-wires generally form two hydrogen bonds per phosphonic functional group because of its diprotic structure. Below we pursue correlations between hydrogen bond strengths and functional group properties such as proton affinities and deprotonation energies.

Density functional theory (BLYP[53,54] and B3LYP[55]) as implemented in Gaussian03, Gaussian Development Version, and Gaussian09[56] was used to compute structures and energies. These were used in conjunction with the following split-valence basis sets: 3-21G,[57−62] 6-311G(d,p),[63,64] cc-pVDZ,[65] cc-pVTZ,[66] and cc-pVQZ.[67] We studied convergence of hydrogen bond strength and wire proton affinity with respect to density functional and basis set for 5-mer wires and as a function of the six proton carrying groups investigated herein. The proton affinity of a wire is defined as the energy difference between the fully optimized unprotonated and protonated wires, where all optimizations are tethered as described above. Below, we find that improving the basis set produces significant changes in energy, while the more complete treatment of electron exchange in B3LYP gives only negligible changes in energy compared to BLYP. We do not have access to the computational resources needed to push these convergence studies to non-DFT-based, post-Hartree−Fock methods such as MP2. However, single-point MP2 proton affinities computed at DFT optimized geometries remained within 0.5% of the DFT results, encouraging the use of a more computationally efficient model chemistry to discern trends. Balancing the convergence results shown below with the need for computational efficiency leads to the following model chemistry used below for long wires: geometry optimization with BLYP/3-21G followed by single-point energy refinement with BLYP/6-311G(d,p). This method is found to be sufficient to obtain hydrogen bond strengths to within 3.7 kJ/mol, and proton affinities to within 12.7 kJ/mol, of values in our most complete model chemistry.

B. Protonated Wires. We investigated proton translocation energetics in various stages. In the first stage, we calculated proton "adsorption" energies by computing the energy difference between structures with the excess charge localized on the end (END) and middle (MID) sites (Figure 6). These calculations were performed on W1 wires of odd lengths in the range 3−19, using propyl linkers and a backbone repeat distance of 5.6 Å. The MID calculations involved full tethered optimization of protonated W1 wires. Because END sites are not local minima, full tethered optimization is not possible in these cases. Instead, we performed a sequence of partial tethered optimizations as follows: (i) keep proton wire fixed at optimal/unprotonated geometry and optimize excess proton location at END site, (ii) keep END N−H bond lengths fixed and optimize remainder of proton wire. As described above, optimizations were performed with BLYP/3-21G, with energies refined at single points with BLYP/6-311G(d,p).

To help interpret the results of these quantum calculations, we also performed electrostatic calculations of proton binding at MID and END sites. We assumed fixed charge−dipole and dipole−dipole interactions with all near-neighbor distances of 5.6 Å, perfectly aligned or anti-aligned dipoles as shown in Figure 6, and an imidazole dipole moment of $\mu_0 = 3.67$ D.[68] For a proton wire of length n, the charge-dipole energy includes $(n-1)$ terms of the form $-e\mu_0/r_i^2$, where e is the proton charge and r_i is the charge−dipole distance. The dipole−dipole energy includes $(n-1)(n-2)/2$ terms of the form $\pm\mu_0^2/r_{ij}^3$, where r_{ij} is the dipole−dipole distance and the $\pm$ arises for anti-alignment/alignment, respectively. We show below that this electrostatic treatment semiquantitatively captures proton embedding energies in imidazole-based proton wires.

Proton binding at MID sites was found to be the ground state for some but not all wires studied herein. As such, we extended our study of proton translocation energetics by searching for the ground states of all protonated C, S, P, N, and W1−W6 wires. All ground-state searches began from the END structure followed by tethered optimization. Some wires optimized through long-range, barrierless Grotthuss shuttling directly to a MID or near-MID structure, while other wires exhibited significant corrugation of the intrawire energy landscape, optimizing to a near-END structure. In these corrugated cases, ground states were sought by localizing an excess proton at each possible binding site and performing a tethered optimization. For selected corrugated systems, we also computed transition states connecting local minima using the Quadratic Synchronous Transit (QST2) procedure.[69,70] These transition states were vibrationally characterized for wires with $n \leq 5$. For longer wires, transition states were confirmed by relaxing along both directions of likely reaction coordinates. Barrier curvatures were found to be in the range $750i-1000i$ cm^{-1} with reduced masses of 1.05 ± 0.01 amu, indicating that proton tunneling becomes important for temperatures below around 200 K using harmonic tunneling theory.[71]

Armed with the END and GROUND states for each wire, we computed the "local" desorption energy defined as $E_{loc} \equiv E_{end} - E_{ground}$. This energy is of interest because it controls transmembrane proton conductivities for relatively thin membranes[72] when the proton source/sink is at the energy E_{end}. We computed local desorption energies for 13-mer C, S, P, N, Im, and Tr linear wires and correlated these with the corresponding functional group proton affinities.

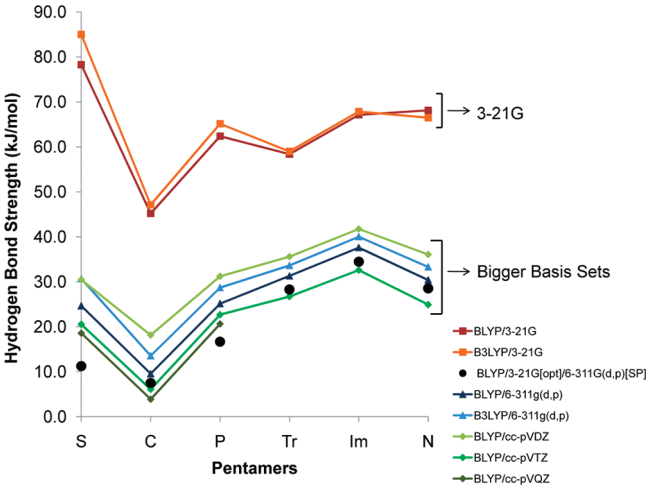

Figure 2. Convergence of hydrogen bond strength (kJ/mol) of pentamers made of functional groups S, C, P, Tr, Im, and N (in increasing order of proton affinity) with respect to level of theory and basis set. Legend: BLYP/3-21G (red); B3LYP/3-21G (orange); BLYP/6-311G(d,p) (dark blue); B3LYP/6-311G(d,p) (light blue); BLYP/cc-pVDZ (light green); BLYP/cc-pVTZ (medium green); BLYP/cc-pVQZ (dark green); BLYP/3-21G[opt]/6-311G(d,p)[SP] (black dots). The basis set effect is more pronounced than the level of theory, with BLYP/3-21G[opt]/6-311G(d,p)[SP] giving hydrogen bond strengths within 3.7 kJ/mol of the best result.

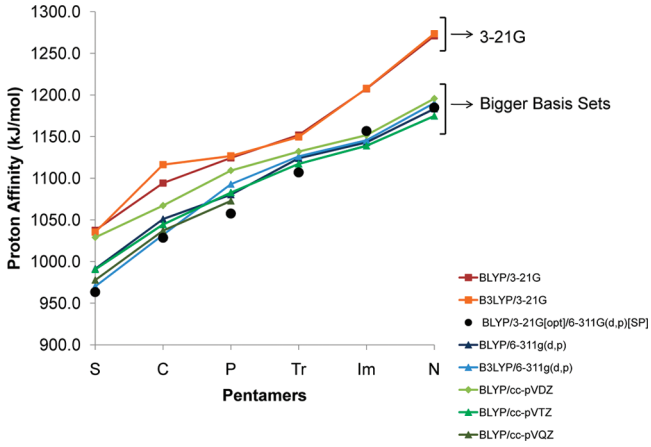

Figure 3. Convergence of proton affinity (kJ/mol) of pentamers made of functional groups S, C, P, Tr, Im, and N with respect to level of theory and basis set. Same legend as in Figure 2. BLYP/3-21G[opt]/6-311G(d,p)[SP] gives proton affinities within 12.7 kJ/mol of the best result.

We also computed "global" proton desorption energies for these 13-mer wires, defined as the proton affinity of each wire. The global desorption energy is of interest because it allows all proton wire energy landscapes to be placed with respect to a common proton source/sink energy, in this case an isolated gas-phase proton. We correlated these global desorption energies with the corresponding functional group proton affinities.

Below we find from geometry optimizations that adding an extra proton to the end of proton wires causes excess charge to embed into the interior segments of proton wires. Because such geometry optimizations correspond to 0 K, it is possible that entropic effects at ambient temperatures lead to qualitatively different results. Indeed, simulations of protonated water clusters at finite temperatures predict that excess charge can equilibrate to the external surfaces of such clusters.[73−75] To investigate whether such phenomena occur in tethered proton wires, we computed thermostatted Born−Oppenheimer ab initio molecular dynamics (AIMD) trajectories[76−78] using Gaussian03/09. Trajectories were computed in a BLYP/6-311G(d,p) model chemistry using a 5-mer W1 wire. Trajectories were initialized with the excess proton localized at the end (first), second, and middle (third) imidazole groups. Each trajectory was initialized with a total nuclear kinetic energy corresponding to a target temperature of 400 K. Fully optimized wave functions were used at each time step separated by 0.3 fs. A thermostat was applied every 50 time steps (15 fs), scaling (but not randomizing) all velocities to reset the nuclear kinetic energy to its initial value. Total energy was conserved to 1 part in 10^7 between applications of the thermostat. After equilibration for 300 fs, trajectories were propagated for another 500−700 fs to confirm equilibration. Subaveraged nuclear kinetic energies obtained from 100 fs slices of these trajectories averaged to a temperature of 399.7 ± 6.4 K. As such, these trajectories convey the equilibrium statistics of a protonated 5-mer near 400 K.

Equilibrium structural properties of such wires were analyzed by tracking the total dipole moments of the protonated wires. As we show below, the total dipole moment serves as a useful reaction coordinate for the cooperative motion of excess charge in these systems.

III. RESULTS AND DISCUSSIONS

We discuss our modeling results in four sections: convergence studies, structures and energies of unprotonated wires, gross energies of protonated wires, and finally, detailed energies and concerted motions in protonated wires.

A. Convergence Studies. The convergence of hydrogen bond strength and wire proton affinity is shown in Figures 2 and 3, respectively (numerical values are tabulated in Supporting Information). We investigated convergence with respect to basis set and density functional (BLYP and B3LYP) for 5-mer wires as a function of all six proton carrying groups. The BLYP and B3LYP calculations with 3-21G and 6-311G(d,p) in Figures 2 and 3 show that improving the basis set is more important for convergence than the level of theory. Indeed, we see that the more complete treatment of electron exchange in B3LYP gives only negligible changes in energy compared to BLYP. It would be prudent to go beyond B3LYP, investigating non-DFT-based, post-Hartree−Fock levels of theory such as MP2. However, we have found for proton siting in zeolites (silica networks) that B3LYP captures about 90% of reaction energies and barriers.[79] As such, these results indicate that BLYP is sufficient to capture the trends we study below.

To pursue convergence with respect to basis set, we used double-ζ basis sets (3-21G, cc-pVDZ), triple-ζ basis sets (6-311G(d,p), cc-pVTZ) and the quadruple-ζ basis set (cc-pVQZ), all with BLYP. We note that cc-pVQZ data were not obtained for the nitrogen-containing functional groups (Tr, Im, and N) because of numerical difficulty in orbital convergence using this basis set. As seen in Figures 2 and 3, all these basis sets give essentially the same trends for hydrogen bond strength and proton affinity versus functional group. To quantify the extent of convergence, we compare the two best available calculations of hydrogen bond strength and proton affinity, i.e., cc-pVQZ/cc-pVTZ for S, C, and P wires and cc-pVTZ/6-311G(d,p) for Tr,

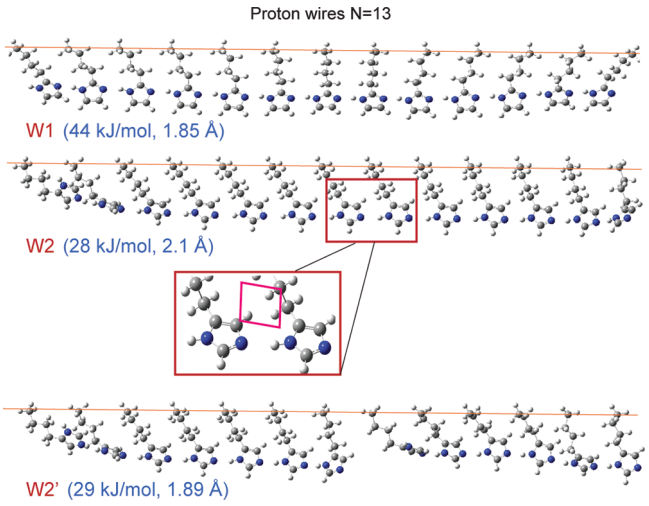

Figure 4. Structures of 13-unit proton wires W1, W2, and W2′ (broken but more stable version of W2). Cohesive energies show relatively strong hydrogen bonding in W1 and W2′. The cause for weaker hydrogen bonds and breaking in W2 (and also W3) is steric repulsions between CH groups in imidazoles (or 1,2,3-triazoles) and adjacent linkers.

Im, and N wires. The average absolute-magnitude-of-difference between these calculations of hydrogen bond strength is 3.6 kJ/mol (maximum 5.5 kJ/mol for the N wire), while that for the proton affinity is 8.3 kJ/mol (maximum 12.8 for the S wire). The hydrogen bond strength is thus converged with respect to a basis set within "chemical accuracy" (within 4 kJ/mol), while the remaining basis set error in proton affinity amounts to less than 0.8% of the mean proton affinity of the six wires studied (1086 kJ/mol). Furthermore, we extended the treatment of electron correlation by computing MP2 single-point energies of the bare and protonated 5-mer wires at the stationary points obtained in a B3LYP/6-311G(d,p) model chemistry. The proton affinity obtained thus is 1159.1 kJ/mol, within 0.2% of the BLYP/6-311G(d,p) value of 1156.6 kJ/mol and within 0.5% of the B3LYP/6-311G(d,p) value of 1164.9 kJ/mol.

The best compromise between convergence and computational efficiency for these systems occurs with a BLYP/6-311G(d,p) model chemistry. The average basis set error between this and the best available result for the hydrogen bond strength is 5.2 kJ/mol, while that for the proton affinity is 9.1 kJ/mol, both quite acceptable errors. However, even full tethered geometry optimizations using BLYP/6-311G(d,p) for the longer wires studied below are beyond our computational resources. We find that sufficiently accurate results can be obtained using BLYP/3-21G optimized geometries with BLYP/6-311G(d,p) single-point corrections, denoted BLYP/3-21G[opt]/6-311G(d,p)[SP]. The differences between this approach and full BLYP/6-311G(d,p) optimizations are 5.3 kJ/mol for hydrogen bond strength and 17.5 kJ/mol for proton affinity. Comparing the BLYP/3-21G-[opt]/6-311G(d,p)[SP] model chemistry to the best available hydrogen bond strengths and proton affinities gives errors of 3.7 and 12.7 kJ/mol, respectively—again, quite acceptable errors. The largest error from using BLYP/3-21G[opt]/6-311G(d,p)-[SP] is found for the hydrogen bond strength of the S wire, which falls from the converged value of 18.6−11.3 kJ/mol. Nonetheless, using BLYP/3-21G[opt]/6-311G(d,p)[SP] produces trends consistent with the more expensive methods, as seen in Figures 2 and 3, and facilitates the study of proton wires with as many as 19 units, allowing the convergence of proton embedding energies with respect to wire length as shown below.

To complete the evaluation of the BLYP/3-21G[opt]/6-311G(d,p)[SP] model chemistry, we analyze the structural differences between BLYP/3-21G and BLYP/6-311G(d,p) optimizations of all the 5-mer wires treated in Figures 2 and 3. Intramolecular and intermolecular N−H and O−H bond lengths and N−H−N and O−H−O angles are tabulated for each of the six wire types in the Supporting Information section. Also included are averages over the length of each wire for each of these quantities and average differences between the two basis sets. In brief, we find that intramolecular N−H and O−H bond lengths differ between the two basis sets by 2% and 5%, respectively. Intermolecular N−H and O−H bond lengths differ by about 10% between the two basis sets, with 3-21G giving consistently shorter hydrogen bonds. Finally, we find that N−H−N and O−H−O angles differ by less than 3%. In the end, we believe this model chemistry provides a practical approach for generating qualitatively accurate chemical trends in longer proton wires.

B. Structures and Energies of Unprotonated Wires. Designing tethered proton wires requires the study of linker length, backbone repeat distance, and functional group properties. As defined above, the optimal linker length gives a proton wire whose proton affinity (PA) is equal to that of an analogous unconstrained system. We studied this for Im trimer wires with a backbone repeat distance of 5.6 Å using B3LYP/6-311G(d,p) because of the small system sizes. PAs were computed for linkers of the form $CH_3-(CH_2)_n-$ for n = 2, 3, 4, and 5. The propyl linker (n = 3) was found to be the shortest alkyl group satisfying the above criterion, with constrained and unconstrained PA values of 1125 and 1121 kJ/mol, respectively. These results show that this linker offers sufficient flexibility to fully accommodate an added proton, in agreement with the simulations of Cavalcanti et al.[32] The propyl linker was used for all calculations reported below.

For each wire type, we determined a range of backbone repeat distances, giving continuous hydrogen-bond networks. Center-of-mass distances between functional groups in dimers optimized with B3LYP/6-311G(d,p) were used as initial values of backbone repeats. For example, Im and Tr dimers were found to be separated by 5.2 Å; continuous proton wires with these groups up to 19 units long were obtained with BLYP/3-21G optimizations using backbone repeats in the range 4.6−5.6 Å. C, N, S, and P wires were found to give continuous hydrogen-bond networks with backbone repeats of 4.3, 4.5, 5.2, and 5.2 Å, respectively. These backbone repeat distances were used for the calculations reported below.

Many synthetically available polymer backbones that provide structural integrity exhibit repeat distances exceeding 6 Å, e.g., polythiophene at 7.9 Å. It is thus of interest to determine the properties of hydrogen-bond networks with backbone repeat distances much greater than optimal values. For Im = W1 13-mer wires optimized with BLYP/3-21G, a repeat distance of 6.0 Å gives a maximum segment length of 9 units, while a 7.9 Å repeat gives only 3 unit segments. This indicates the unsuitability of polythiophene for scaffolding linear Im proton wires.

Interdigitation offers an alternative structural motif for forming proton wires, as depicted in Figure 1b. We studied this motif in 3-mer wires W4, W5, and W6, keeping the backbone distance of 7.9 Å fixed and setting the isosceles triangle interscaffold distance d to 5.7, 7.9, and 10.0 Å (see Figure 1b). All these

dx.doi.org/10.1021/jp1051535 |J. Phys. Chem. A 2011, 115, 5423–5434

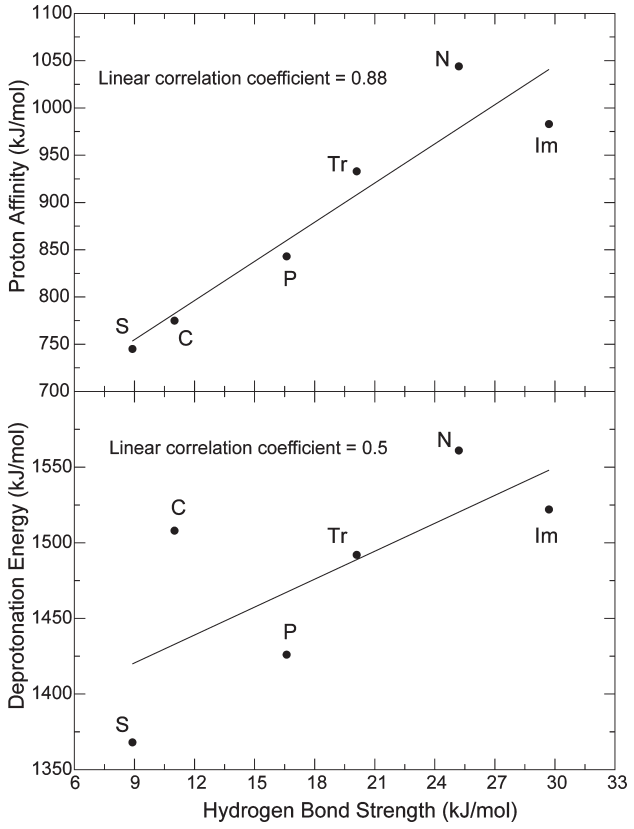

Figure 5. Proton wire hydrogen bond strengths correlated with two computed functional group properties: proton affinity (PA) and deprotonation energy. Hydrogen bond strength is found to correlate much better with PA, indicating hydrogen bonding in neutral wires is dominated by proton addition with minimal deprotonation character.

systems were found to produce continuous networks despite the long 7.9 Å repeat distance in each linear scaffold. The structure with a 7.9 Å interscaffold distance, which gives an equilateral triangle of fixed atoms, was found to give the most stable proton wires for W4, W5, and W6 systems. This equilateral interdigitation scheme was used for the calculations below on W4, W5, and W6 wires.

Figure 4 shows structures, cohesive energies, and average hydrogen-bond distances for optimized 13-mer W1 and W2 wires, which are identical except for the imidazole attachment point. The average hydrogen-bond strengths in W1 and W2 are 48 and 30 kJ/mol, respectively. To put these bond strengths into perspective, we note that the normalized dipole−dipole energy of 13 perfectly aligned imidazole dipoles (3.67 D) separated by 5.6 Å is only 4.8 kJ/mol, indicating that the actual wires are stabilized by chemical effects. Indeed, atomic charges extracted from electrostatic potential fitting (ESP charges) indicate that each monomer in these 13-mer wires carries a small net charge (±0.1e), indicating small amounts of charge transfer between neighboring groups.

Although hydrogen bonding in both wires is found to be quite strong, it is weaker in W2 because of steric interactions between imidazole and linker CH groups. This effect produces a complex landscape of proton wire minima in W2 (and also in W3). Figure 4 shows a discontinuous structure of W2 denoted W2′ with one less hydrogen bond, which is just as stable as the continuous wire because W2′ can form shorter hydrogen bonds. Upon decreasing the backbone repeat distance to 5.2 and 4.8 Å for both W2 and W3, broken wires were still observed as ground states. This persistent degeneracy in proton wire structure has implications for proton translocation, which we discuss below.

For all 13-mer proton wires studied, mean hydrogen bond distances were found to range from 1.5 Å (C-wire) to 2.2 Å (W3), while mean hydrogen bond strengths vary from 9 kJ/mol (S-wire) to 51 kJ/mol (W4) using BLYP/3-21G[opt]/6-311G(d,p)[SP]. (All hydrogen bond strengths and distances are provided as Supporting Information.) It is interesting to correlate this broad range of hydrogen bond strengths with functional group properties such as proton affinity (PA) and deprotonation energy, which describe the gain and loss of a proton, respectively, as occurs in hydrogen bonding. Note that we do not pursue correlations with the pK_a, which is the deprotonation free energy in water (divided by 2.3RT). This is because the pK_a can represent an ensemble of structures not present in our proton wires. For example, formic acid partially dimerizes in water;[80] in addition, sulfonic acid exists as both monoprotic and diprotic isomers, while the S-wire contains only the monoprotic form. Correlating with our calculated PAs and deprotonation energies avoids these inappropriate comparisons.

Figure 5 shows functional group PAs and deprotonation energies (optimized with BLYP/6-311G(d,p)) versus 13-mer proton wire hydrogen bond strengths (computed with BLYP/3-21G[opt]/6-311G(d,p)[SP]). Figure 5 shows that while the correlation with deprotonation energy is quite poor it is much better with PA showing a linear correlation coefficient of 0.88. This indicates that hydrogen bonding in these wires is dominated by proton *addition*, with minimal deprotonation character. Indeed, intramolecular NH and OH bond lengths increase only slightly from monomer values in the range 0.98−1.03 Å, to average wire values of 1.04−1.09 Å (see Supporting Information for all values).

To put this result in context, we note that previous computational studies have investigated relations between PA and binding energy of proton-bound homodimers $[A\cdots H{-}A]^+$[45] and heterodimers $[A\cdots H{-}B]^+$.[46−51] Heterodimer stability was found to increase as the PA difference of A and B decreases, with homodimers being the most stable[46−51] and the most relevant to the present study of homodromic proton wires. Chan et al. found that the binding energies of such $[A\cdots H{-}A]^+$ species (relative to energies of $[H{-}A]^+$ and A) follow non-monotonic, quadratic dependencies on PA. Homodimer stability was found to increase with increasing PA for molecules with low PA values, reach a maximum stability for intermediate PA values, and then decrease in stability for high PA values as $[H{-}A]^+$ exhibits partial deprotonation.

In contrast, we find a monotonic, approximately linear correlation between hydrogen bond strength and functional group PA. The principal difference between our work and that of Chan et al.—beyond the fact that we studied longer, tethered hydrogen bond networks—is that Figure 5 pertains to *neutral* systems, whereas Chan et al. studied protonated dimers. Our study of hydrogen bond strengths in neutral wires is motivated by the fact that proton densities in polymer conductors are likely to be relatively low, suppressed by Coulombic repulsion between proximal protons in a low-dielectric environment. As such, the processes of proton wire formation and regeneration are likely more sensitive to neutral hydrogen bond strengths. The fact that we observe minimal deprotonation character in neutral wires, even for the highest PA values considered (1000 kJ/mol),

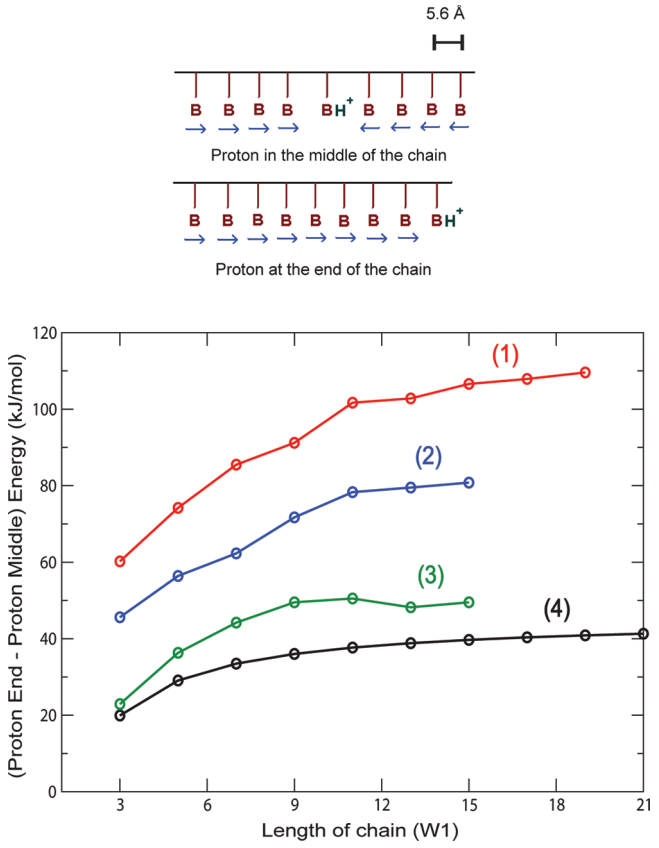

Figure 6. Difference in energies between protonated W1 wires with excess proton at END and MID sites, as a function of W1 wire length. In all cases MID is the predicted ground state of W1. END energies computed as: (1) single-point BLYP/3-21G (red); (2) single-point BLYP/6-311G(d,p) (blue); (3) tethered optimization with excess proton fixed at end, optimized with BLYP/3-21G, and refined using BLYP/6-311G(d,p) (green); (4) electrostatic theory (black). (1) to (2) shows the basis set effect; (2) to (3) shows the effect of relaxating protons close to excess proton; and (3) to (4) shows the success of electrostatic theory capturing proton embedding energy.

explains why we observe a monotonic correlation between hydrogen bond strength and PA.

This observation of PA-controlled hydrogen bond strength provides a new criterion for tuning the properties of proton wires. Indeed, Figure 5 indicates that P and Tr wires exhibit intermediate hydrogen bond strengths, which may optimize the balance between alignment of functional groups for efficient proton shuttling and orientational flexibility of functional groups for rapid regeneration. We believe that a qualitatively similar trend also exists for the hydrogen bond free energy, taking entropy into account. This is because each functional group loses translational entropy upon hydrogen bonding. In addition, the groups that exhibit weaker hydrogen bonding (sulfonic, formic, and phosphonic acids in Figure 5) also lose some torsional entropy upon hydrogen bonding, thus reinforcing the trend shown in Figure 5. We will pursue these ideas with future molecular dynamics simulations on these wire types.

C. Gross Energies of Protonated Wires. From a coarse-grained perspective, hydrogen bond networks can be viewed as a series of locally aligned dipoles. Adding a proton to such networks can interfere with dipolar alignment, raising the question about the most stable location for excess charge. Many studies have been reported on the fates of excess charge in bulk water and water clusters,[1,2,6,7,9,10,25,34,81,82] exploring whether excess charge stabilizes as surface or embedded species. Focusing on enthalpic effects, dipole−dipole energies tend to push excess charge to surfaces, while charge−dipole energies tend to embed charge in bulk. We investigated the analogous question for a proton added to Im (W1) wires of various lengths, by computing the energies of protonated wires at middle (MID) and end (END) states as depicted in Figure 6. Our results show that for all wire lengths and levels of theory MID states are more stable, indicating that for these wires charge−dipole energies drive proton embedding at 0 K. A qualitatively similar result was obtained by Hummer and co-workers for aqueous proton wires confined in carbon nanotubes.[9−12]

Figure 6 shows four approaches for calculating the proton embedding energy $E_{end} - E_{mid}$. Because the embedded proton was found to be the ground state in all cases, E_{mid} can be obtained by full tethered optimization. In contrast, determining E_{end} requires some form of constraint to localize a proton at the wire's end. To do this, we considered the following approaches:

1. BLYP/3-21G Constrained End State
   - E_{mid}: BLYP/3-21G full tethered optimization.
   - E_{end}: BLYP/3-21G single-point calculation of an excess proton attached to a previously optimized W1 wire.
2. BLYP/6-311G(d,p) Constrained End State
   - E_{mid}: BLYP/3-21G[opt]/6-311G(d,p)[SP] full tethered optimization.
   - E_{end}: BLYP/6-311G(d,p) single-point calculation of an excess proton attached to a previously optimized W1 wire.
3. BLYP/6-311G(d,p) Relaxed End State
   - E_{mid}: BLYP/3-21G[opt]/6-311G(d,p)[SP] full tethered optimization.
   - E_{end}: BLYP/3-21G[opt]/6-311G(d,p)[SP] full tethered optimization except with both NH bond lengths fixed in terminal Im.
4. Electrostatics calculation using dipole−dipole and charge−dipole energies as described above, with excess charge localized at MID and END states.

Comparing these methods provides insight into proton embedding in these systems. Method 1 appears to reach a plateau embedding energy of about 110 kJ/mol. This same embedding energy scale (100 kJ/mol) was found at this level of theory for all Im- and Tr-based wires studied herein (wires W1−W6). Comparing (1) and (2) shows that improving the basis set reduces proton embedding energies by 20−25%. Comparing (2) and (3) shows that relaxing proton wires in END states reduces embedding energies even further by as much as 30 kJ/mol, leading to our final prediction of W1 embedding energies on the order of 40 kJ/mol. A substantial amount of this relaxation comes from distorted hydrogen bonds close to the added proton. The agreement between (3) and (4) indicates that, although simple electrostatics does not predict hydrogen bond strengths in these systems, they account for proton embedding energies semiquantitatively. This augurs well for the use of force fields to model proton dynamics, which will be pursued in future work.

To investigate whether proton embedding occurs under ambient conditions (at finite temperatures), we performed ab initio molecular dynamics (AIMD) simulations near 400 K on 5-mer W1 wires, with an excess proton initiated at the end and middle sites. To quantify the statistics of proton siting under

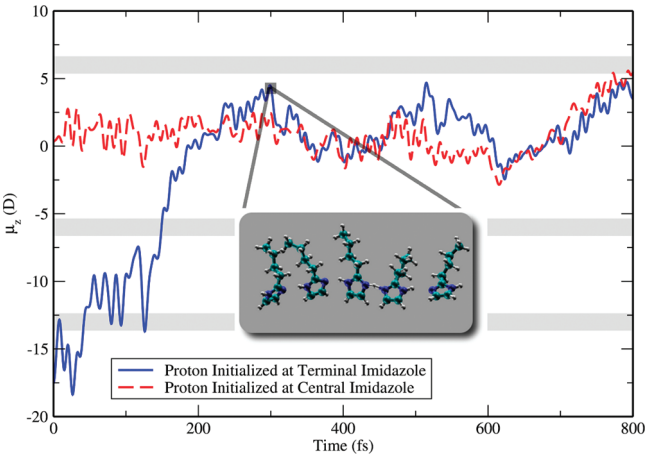

Figure 7. Representative ab initio molecular dynamics trajectories near 400 K of protonated 5-mer W1 wires, showing the dipole moment projection along the tethering axis (μ_z). Gray bars show values of μ_z when excess charge is approximately shared between neighboring sites, serving as "bin boundaries" that localize excess charge at individual monomer sites. The trajectory initiated at the wire center fluctuates about this state with no large-amplitude motion. In contrast, the run initiated at the wire terminus exhibits a large-amplitude equilibration process to the central site, in agreement with geometry optimizations. The inset displays the geometry at one of the largest amplitude excursions about equilibrium.

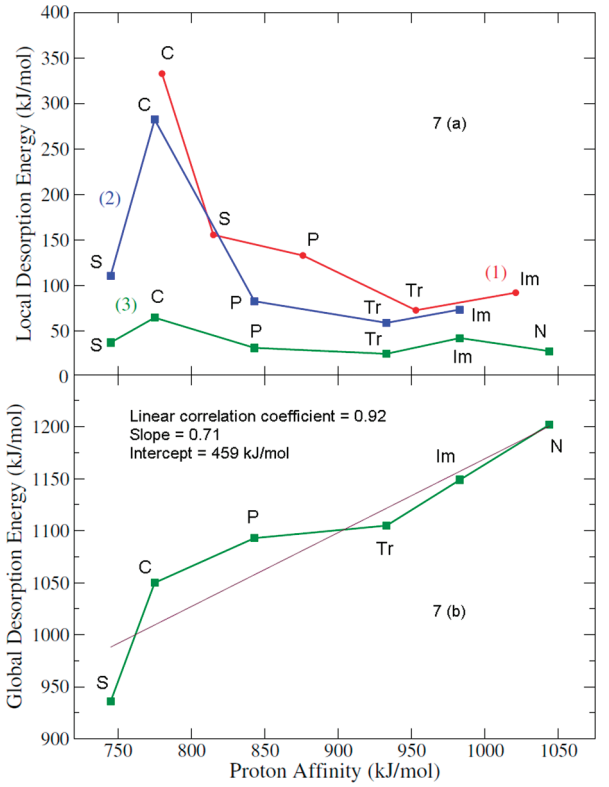

Figure 8. (a) Local desorption energy ($E_{end} - E_{ground}$) versus proton affinity (PA). Methods (1), (2), and (3) are the same as in Figure 6. Using the most accurate approach, method (3), the local desorption energy is found to be roughly independent of functional group PA, showing that proton desorption from wires is a collective process. (b) Global desorption energy (proton affinity of each wire) versus functional group PA. These correlate well precisely because the local desorption energy is roughly constant.

ambient conditions, we tracked the component of the dipole moment of a protonated wire parallel to its tethering axis. This quantity should have a value near zero when excess charge is symmetrically localized at the central site and a large magnitude when the proton is localized at a terminal site. To test the usefulness of this dipole as a reaction coordinate, we performed three constrained optimizations on 5-mer W1 wires using B3LYP/6-311G(d,p), with an excess proton constrained to sites 1, 2, or 3. We found the component of the dipole along the tethering axis (μ_z) to have magnitudes of 18.0, 8.7, and 3.5 D, respectively, at these three sites, indicating a monotonic relationship between dipole moment and excess-charge location. Furthermore, binning of N−H distances from the AIMD trajectories reveals an excellent correspondence between μ_z and proton siting, with dipole moment ranges of 13−18 D obtained when the proton is at the terminal group, 8−13 D when excess charge visits the second imidazole, and 0−8 D when excess charge vibrates around the central imidazole. The magnitudes of these dipole ranges (5−8 D) reflect the anharmonic nature of hydrogen bond network vibrations in these wires. Thus, these results demonstrate that the continuous variable μ_z serves as a useful reaction coordinate for cooperative proton shuttling in these systems.

Figure 7 displays the variation in μ_z over 800 fs for two AIMD trajectories, one initialized with excess charge at the terminal imidazole and the other at the central site. In the model chemistry used [BLYP/6-311G(d,p)], the central site is the ground state, more stable than the terminus by ~40 kJ/mol. In the trajectory initialized at the ground state (central group), the excess charge is found to execute only small amplitude excursions along the wire, moving no more than one monomer unit from the starting configuration and usually much less than that. In contrast, the trajectory initialized with an excess proton at the wire terminus was found to undergo a large-amplitude equilibration. In this process, the system undergoes a small number of N−H vibration cycles shown by μ_z fluctuating around 16 D before undergoing a discrete "hop" to the neighboring monomer. From 50 to 150 fs, the excess charge remains localized at the second monomer, experiencing N−H vibrations seen as fluctuations in μ_z around 11 D, followed by another discrete "hop" to the central monomer, after which the system exhibits equilibrium fluctuations essentially identical to those of the trajectory initialized at the central imidazole. These AIMD results suggest that the qualitative conclusions drawn from the 0 K geometry optimizations described above are consistent with equilibrium proton siting at elevated temperatures.

The MID state was found to be the ground state for all protonated W1 wires; this is not the case for all wires. Using the methods outlined above, we determined the ground state energies for all protonated wires using full tethered optimization. We then determined END energies for these protonated wires with methods (1), (2), and (3) above, using the same basis set for END and ground states. The local desorption energy defined as $E_{loc} \equiv E_{end} - E_{ground}$ was then computed and correlated with the PA of each functional group, as shown in Figure 8a. Method (1) exhibits a surprising anticorrelation with functional group. This anticorrelation essentially disappears with (2) a bigger basis set and (3) END-state wire relaxation, giving local desorption energies that are remarkably uniform among the wires (44 ± 18 kJ/mol). As we show below, the lack of corrugation in the

potential energy surface for proton motion through continuous wires makes this local desorption energy key for controlling translocation rates. The fact that these desorption energies show no correlation with functional group properties suggests that proton desorption is a collective process in proton wires.

Proton conductivities are the product of concentration and mobility. While the local desorption energy sheds light on mobility, it lacks a consistent thermodynamic reference state needed for elucidating concentration effects. Instead, the global desorption energy, defined as the proton affinity of each wire, provides the common reference state of a gas-phase proton with zero energy. The proton affinity is given by $E_{\mathrm{unprot-wire}} - E_{\mathrm{ground}}$, where $E_{\mathrm{unprot-wire}}$ is the optimized energy of an unprotonated wire and E_{ground} is the ground state energy of a protonated wire.

Global desorption energies are shown in Figure 8b versus group PA values, revealing a very good correlation. Given the findings reported above, this correlation should be expected for the following reasons. The global desorption energy can be decomposed into the proton affinity of the END state and the embedding energy to the ground state. This embedding energy is just the local desorption energy, which was found above to be relatively uniform among the wires studied herein. It is reasonable to assume that the proton affinity of the END state closely follows the functional group PA, modulo wire relaxation effects. As such, the proton affinity of the wire is approximately the functional group proton affinity plus a roughly constant embedding energy. Indeed, the small deviations from constancy in Figure 8a mirror the small deviations from linearity in Figure 8b. Thus, we find that the thermodynamic likelihood of wire protonation correlates closely with the functional group proton affinity.

D. Detailed Energies and Concerted Motions in Protonated Wires. Proton translocation involves three basic steps: proton addition to the wire, proton diffusion across the wire, and proton desorption from the wire. Here we address the competition between proton diffusion and desorption rates in proton wires, by computing the landscape of minima and transition states controlling proton motion in wires W1−W6. Because of the substantial computational expense involved, all these calculations were performed using BLYP/3-21G, giving local desorption energies on the order of 100 kJ/mol as discussed above. BLYP/3-21G[opt]/6-311G(d,p)[SP] desorption energies are closer to 40 kJ/mol, e.g., 42 kJ/mol for W1. Figure 9 shows the detailed energetics for linear wires W1−W3, while Figure 10 shows the same for interdigitated wires W4−W6, with local minima shown as thick dots and transition states as solid lines. All energies (kJ/mol) are relative to the ground state of each protonated wire. Figure 9 shows that for W1 the potential energy landscape for intrawire proton diffusion is extremely flat with site-to-site barriers less than 10 kJ/mol. This is in excellent agreement with the apparent activation energy for proton diffusion in liquid imidazole simulated by Voth and co-workers,[33] suggesting that proton diffusion in W1 rivals that in the untethered imidazole liquid.

These small barriers for proton motion in W1 indicate that for short wires proton translocation through W1 is desorption-limited. For longer wires, diffusion times grow, with the crossover occurring when $k_{\mathrm{des}}L^2/D = 1$, where k_{des} and D are desorption and diffusion constants, respectively, and L is wire length. To estimate the crossover length we assume Arrhenius temperature dependencies $k_{\mathrm{des}} = A_{\mathrm{des}} \cdot e^{-E_{\mathrm{des}}/RT}$ and $D = A_{\mathrm{dif}} \cdot e^{-E_{\mathrm{dif}}/RT} \cdot a^2$, where A_i are prefactors, $E_{\mathrm{des}} = 42$ kJ/mol and $E_{\mathrm{dif}} = 10$ kJ/mol as found above for W1; RT is thermal energy; and a is the site-to-site proton hop length. Assuming that the prefactors cancel, the room-temperature crossover value of (L/a) is given by $e^{(42-10)/5} = 601.8 \cong 600$ units. As such, we predict that proton translocation through W1 is diffusion limited for hydrogen bond networks longer than 600 units and otherwise desorption limited. We note that persistence lengths in conjugated polymers, possible scaffolds for proton wires, vary from 2 to 10 nm,[83−85] a distance range much shorter than 600 imidazole groups. Thus, we predict that with such scaffolds proton translocation will be desorption limited in imidazole-based wires.

Figure 9 shows much greater corrugation in the energy landscape of proton motion through W2 and W3, arising from the tendency in these wires to break into shorter segments. As

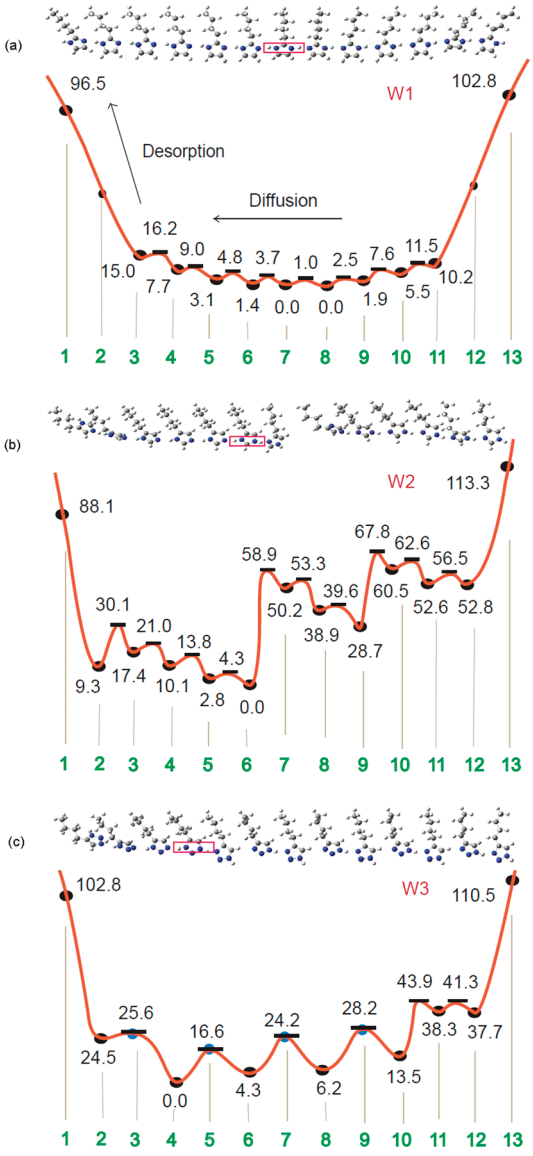

Figure 9. Proton translocation potential energy surfaces (BLYP/3-21G) of (a) W1, (b) W2, and (c) W3 13-mer wires. W1 has 9 minima connected by rather low barriers, indicating rapid intrawire motion rivaling that in liquid imidazole. The mechanism of proton translocation is predicted to be desorption limited. W2 and W3 have 11 and 7 minima, respectively, connected by high barriers because of wire breakage caused by proton translocation, showing the importance of the functional group attachment point.

dx.doi.org/10.1021/jp1051535 |J. Phys. Chem. A 2011, 115, 5423–5434

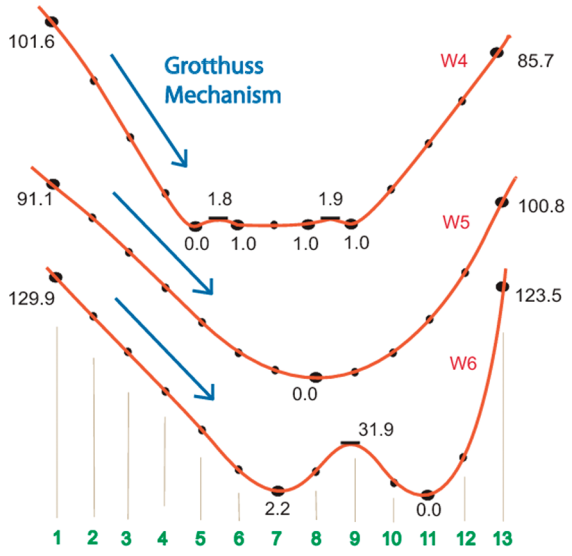

Figure 10. Proton translocation potential surfaces for W4, W5, and W6 13-mers (interdigitated versions of W1−W3) using BLYP/3-21G. These wires exhibit fewer minima compared to the corresponding linear wires W1−W3, with long-range (35 Å) Grotthuss shuttling as the mechanism of proton relaxation in W5.

discussed above, this tendency is caused by steric interactions between functional group and linker CH groups that weaken the hydrogen bond network. Although we expect longer translocation times for protons through W2 and W3, regenerating these wires for subsequent protons may be more facile than in W1. In future work, we will investigate the balance between these effects using molecular dynamics simulations.

Figure 10 shows the corresponding energy landscapes for proton motion through the interdigitated wires W4−W6, exhibiting strikingly different characteristics. Whereas W1 exhibits 9 minima connected by small barriers, the corresponding W4 has only 4 minima with negligible barriers. Whereas W2 exhibits 11 minima connected by many large barriers, W5 has only *one single minimum* at imidazole number 8. As such, protonating W5 at group 1 produces a cascade of Grotthuss shuttling culminating in an excess charge roughly 35 Å away from the added proton (see Supporting Information for animation of Grotthuss shuttling in W5). Long-range shuttling is active in W4, W5, and W6 but is most pronounced in W5.

These results suggest that, for imidazole- and triazole-based wires, interdigitation promotes longer-range Grotthuss shuttling than in the corresponding linear wires. Although more work is needed to fully understand the origin of this effect, relatively simple experiments can test our predictions. For example, proton conductivities measured from imidazole-based polymers with various backbone repeat distances should reveal the interdigitation effect. If the backbone distance is 5.6 Å, only linear wires should form, while a different backbone with a 7.9 Å repeat would only allow interdigitated wires to form. Interdigitation is also a natural mechanism for interwire transport and thus should produce significantly higher conductivities.

IV. SUMMARY AND CONCLUDING REMARKS

We have modeled structures and energetics of anhydrous proton wires of the form ···HX···HX···HX···, with functional groups HX = imidazole, triazole, and formamidine; formic, sulfonic, and phosphonic acids. We have performed a convergence study of proton wire stability and protonation energies using BLYP and B3LYP density functionals, with basis sets 3-21G, 6-311G(d,p), cc-pVDZ, cc-pVTZ, and cc-pVQZ. We found that BLYP/3-21G optimizations corrected with single-point BLYP/6-311G(d,p) is sufficient to obtain hydrogen bond strengths to within 3.7 kJ/mol, and proton affinities to within 12.7 kJ/mol, of converged values. We have used this model chemistry to study proton wires up to 19 units long, where each proton carrier is linked to an effective backbone to mimic polymer tethering. This approach allows the direct calculation of hydrogen bond strengths. The proton wires were found to be stabilized by strong hydrogen bonds (up to 50 kJ/mol) whose strength correlates with the proton affinity of HX [related to $pK_b(HX)$], and not to $pK_a(HX)$ as is often assumed. Wires based on triazole and phosphonic acid exhibit intermediate hydrogen bond strengths that may optimize the balance between alignment of hydrogen bonds and flexibility for proton wire regeneration.

We have found that propyl linkers, various backbone repeat distances, and interdigitated proton wire architectures promote long-range Grotthuss shuttling in these networks. Ab initio molecular dynamics on imidazole-based wires near 400 K agree with corresponding geometry optimizations, predicting that adding a proton to the end of such wires causes the excess charge to embed into the interior segments of these wires. Proton energy landscapes calculated with DFT suggest that proton translocation is controlled by the energetics of desorption from the proton wire, even for relatively long wires (e.g., 600 imidazole units), with desorption energies of the order of 40 kJ/mol for all the wires studied herein. These proton desorption energies show no correlation with functional group properties, suggesting that proton desorption is a collective process in proton wires. Furthermore, despite the tethering of functional groups, we find long-range Grotthuss shuttling for distances as long as 42 Å in the molecular wires studied above, especially for interdigitated architectures. We predict that, for imidazole- and triazole-based proton wires, tuning the backbone repeat distance from 5 Å (linear) to 8 Å (interdigitated) will show that interdigitation produces faster conduction.

Despite these conclusions, many questions remain unanswered regarding the role of multiprotonated wires, the dynamics of counterions and flexible backbones, and the impacts of thermal fluctuations and wire regeneration. Answering these questions will give a fuller view for optimizing next-generation solid-state proton conductors.

■ ASSOCIATED CONTENT

Supporting Information. Data for convergence of hydrogen bond strength and wire proton affinity with respect to basis set for all the pentamer wires, Cohesive Energies (CE), Hydrogen Bond Strength, Local Desorption Energy (LDE), Global Desorption Energy (GDE) for all thirteen unit wires, average intermolecular and intramolecular hydrogen bond distances for the thirteen unit wires (also their corresponding min/max), and the intramolecular N−H/O−H distances in the monomer/protonated monomer, intramolecular and intermolecular N−H/O−H distances, and N−H−N/O−H−O angles for pentamers W1, W2, Tr, N, C, S, and P and their averages over the length of each wire for each of these quantities. Also, average differences between the two basis sets 3-21G and 6-311G(d,p)

are provided. This material is available free of charge via the Internet at http://pubs.acs.org.

AUTHOR INFORMATION

Corresponding Author
*E-mail: auerbach@chem.umass.edu.

ACKNOWLEDGMENT

We acknowledge generous funding from the National Science Foundation Center for Chemical Innovation Program (CHE-0739227). We thank all members of the UMass Fueling the Future Center for Chemical Innovation for stimulating discussions on charge transfer. SMA thanks Prof. Horia Metiu and the UCSB Department of Chemistry for providing an ideal environment for completing this manuscript.

REFERENCES

(1) Markovitch, O.; Chen, H.; Izvekov, S.; Paesani, F.; Voth, G. A.; Agmon, N. *J. Phys. Chem. B* **2008**, *112*, 9456–9466.
(2) Chen, H.; Voth, G. A.; Agmon, N. *J. Phys. Chem. B* **2010**, *114*, 333–339.
(3) Narayan, S.; Wyatt, D. L.; Crumrine, D. S.; Cukierman, S. *Biophysical* **2007**, *93*, 1571–1579.
(4) Raghavender, U. S.; Aravinda, S.; Shamala, N.; Kantharaju,; Rai, R.; Balaram, P. *J. Am. Chem. Soc.* **2009**, *131*, 15130–15132.
(5) Cukierman, S. *Front. Biosci.* **2003**, *8*, 1118–1139.
(6) Pomés, R.; Roux, B. *Biophys. J.* **1998**, *75*, 33–40.
(7) Pomés, R.; Roux, B. *Biophys. J.* **2002**, *82*, 2304–2316.
(8) Lee, Y.; Martin, C. D.; Parise, J. B.; Hriljac, J. A.; Vogt, T. *Nano Lett.* **2004**, *4*, 619–621.
(9) Dellago, C.; Naor, M. M.; Hummer, G. *Phys. Rev. Lett.* **2003**, *90*, 105902–1.
(10) Dellago, C.; Hummer, G. *Phys. Rev. Lett.* **2006**, *97*, 245901–1.
(11) Köfinger, J.; Hummer, G.; Dellago, C. *J. Chem. Phys.* **2009**, *130*, 154110–1.
(12) Köfinger, J.; Hummer, G.; Dellago, C. *Proc. Natl. Acad. Sci. U.S.A.* **2008**, *105*, 13218–13222.
(13) Drukker, K.; Hammes-Schiffer, S. *J. Chem. Phys.* **1997**, *107*, 363–374.
(14) Drukker, K.; de Leeuw, S.; Hammes-Schiffer, S. *J. Chem. Phys.* **1998**, *108*, 6799–6808.
(15) Marx, D. *ChemPhysChem* **2006**, *7*, 1848–1870.
(16) D. Marx abd, M. E.; Tuckerman, J. H.; Parrinello, M. *Nature* **1999**, *397*, 601–604.
(17) Berkelbach, T. C.; Lee, H.; Tuckerman, M. E. *Phys. Rev. Lett.* **2009**, *103*, 238302–4.
(18) Habenicht, B. F.; Paddison, S. J.; Tuckerman, M. E. *J. Mater. Chem.* **2010**, *20*, 6342–6351.
(19) Habenicht, B. F.; Paddison, S. J.; Tuckerman, M. E. *Phys. Chem. Chem. Phys.* **2010**, *12*, 8728–8732.
(20) Choe, Y.; Tsuchida, E.; Ikeshoji, T.; Yamakawab, S.; Hyodo, S. *Phys. Chem. Chem. Phys.* **2009**, *11*, 3892–3899.
(21) Choe, Y.; Tsuchida, E.; Ikeshoji, T.; Ohira, A.; Kidena, K. *J. Phys. Chem. B* **2010**, *114*, 2411–2421.
(22) Kreuer, K. D. *Annu. Rev. Mater. Res.* **2003**, *33*, 333–359.
(23) Schuster, M. F. H.; Meyer, W. H. *Ann. Rev. Mater. Res.* **2003**, *33*, 233.
(24) Kreuer, K. D.; Paddison, S. J.; Spohr, E.; Schuster, M. *Chem. Rev.* **2004**, *104*, 4637–4678.
(25) Iannuzzi, M.; Parrinello, M. *Phys. Rev. Lett.* **2004**, *93*, 02590.
(26) Bureekaew, S.; Horike, S.; Higuchi, M.; Mizuno, M.; Kawamura, T.; Tanaka, D.; Yanai, N.; Kitagawa, S. *Nat. Mater.* **2009**, *8*, 831–836.
(27) Lee, H.; Tuckerman, M. E. *J. Phys. Chem. C* **2008**, *112*, 9917–9930.
(28) Wood, B. C.; Marzari, N. *Phys. Rev. B* **2007**, *76*, 134301.
(29) Roudgar, A.; Narasimachary, S. P.; Eikerling, M. *Chem. Phys. Lett.* **2008**, *457*, 337–341.
(30) Vilciauskas, L.; Paddison, S. J.; Kreuer, K. *J. Phys. Chem. A* **2009**, *113*, 9193–9201.
(31) Joswig, J.; Hazebroucq, S.; Seifert, G. *J. Mol. Struct.: THEOCHEM* **2007**, *816*, 119–123.
(32) Cavalcanti, W. L.; Marschall, R.; Tölle, P.; Köhler, C.; Wark, M.; Frauenheim, T. *Fuel Cells* **2008**, *08*, 244–253.
(33) Chen, H.; Yan, T.; Voth, G. A. *J. Phys. Chem A* **2009**, *113*, 4507–4517.
(34) Brédas, J. L.; Poskin, M. P.; Delhalle, J.; André, J. M. *J. Phys. Chem.* **1984**, *88*, 5882–5887.
(35) Chuang, S. W.; Hsu, S. L. C.; Yang, M. L. *Eur. Polym. J.* **2008**, *44*, 2202–2206.
(36) Li, Q. F.; Jensen, J. O.; Savinell, R. F.; Bjerrum, N. J. *Prog. Polym. Sci.* **2009**, *34*, 449–477.
(37) Woudenberg, R. C.; Yavuzcetin, O.; Tuominen, M. T.; Coughlin, E. B. *Solid State Ionics* **2007**, *178*, 1135–1141.
(38) Martwiset, S.; Woudenberg, R. C.; Granados-Focil, S.; Yavuzcetin, O.; Tuominen, M. T.; Coughlin, E. B. *Solid State Ionics* **2007**, *178*, 1398–1403.
(39) Martwiset, S.; Yavuzcetin, O.; Versek, C.; Thorn, M.; Tuominen, M. T.; Coughlin, E. B. *J. Polym. Sci, Part A: Polym. Chem.* **2009**, *47*, 188–196.
(40) Subbaraman, R.; Ghassemi, H.; Zawodzinski, T. *Solid State Ionics* **2009**, *180*, 1143–1150.
(41) de Grotthuss., C. J. T. *Ann. Chim.* **1806**, *58*, 54–73.
(42) Agmon, N. *Chem. Phys. Lett.* **1995**, *244*, 456–462.
(43) Subbaraman, R.; Ghassemi, H.; Zawodzinski, T. *J. Am. Chem. Soc.* **2007**, *129*, 2238.
(44) Deng, Q.; Molinero, V.; Goddard, W. *J. Am. Chem. Soc.* **2004**, *126*, 15644–15645.
(45) Chan, B.; Del Bene, J. E.; Radom, L. *J. Am. Chem. Soc.* **2007**, *129*, 12197–99.
(46) Bian, L. *J. Phys. Chem. A* **2003**, *107*, 11517–24.
(47) Singh, P. C.; Patwari, N. *J. Phys. Chem. A* **2007**, *111*, 3178–83.
(48) Özen, A. S.; Proft, F. D.; Aviyente, V.; Geerlings, P. *J. Phys. Chem. A* **2006**, *110*, 5860–68.
(49) Lutz, H. D. *J. Mol. Struct.* **2003**, *646*, 227–236.
(50) Gilli, P.; Pretto, L.; Gilli, G. *J. Mol. Struct.* **2007**, *844−845*, 328–339.
(51) Gilli, P.; Gilli, G. *J. Mol. Struct.* **2010**, *972*, 2–10.
(52) Woudenberg, R. C.; Tuominen, M. T.; Coughlin, E. B. *Solid State Ionics* **2007**, *178*, 1135–1141.
(53) Becke, A. D. *Phys. Rev. A* **1988**, *38*, 3098.
(54) Lee, C.; Yang, W.; Parr, R. G. *Phys. Rev. B* **1988**, *37*, 785.
(55) Becke, A. D. *J. Chem. Phys.* **1993**, *98*, 5648–5652.
(56) Frisch, M. J. *Gaussian 09*, revision A.1; Gaussian Inc.: Wallingford CT, 2009.
(57) Binkley, J. S.; Pople, J. A.; Hehre, W. J. *J. Am. Chem. Soc.* **1980**, *102*, 939–947.
(58) Gordon, M. S.; Binkley, J. S.; Pople, J. A.; Pietro, W. J.; Hehre, W. J. *J. Am. Chem. Soc.* **1982**, *104*, 2797–2803.
(59) Pietro, W. J.; Francl, M. M.; Hehre, W. J.; Defrees, D. J.; Pople, J. A.; Binkley, J. S. *J. Am. Chem. Soc.* **1982**, *104*, 5039–5048.
(60) Dobbs, K. D.; Hehre, W. J. *J. Comput. Chem.* **1986**, *7*, 359–378.
(61) Dobbs, K. D.; Hehre, W. J. *J. Comput. Chem.* **1987**, *8*, 861–879.
(62) Dobbs, K. D.; Hehre, W. J. *J. Comput. Chem.* **1987**, *8*, 880–893.
(63) McLean, A. D.; Chandler, G. S. *J. Chem. Phys.* **1980**, *72*, 5639–5648.
(64) Raghavachari, K.; Binkley, J. S.; Seeger, R.; Pople, J. A. *J. Chem. Phys.* **1980**, *72*, 650–654.
(65) Dunning, T. H., Jr. *J. Chem. Phys.* **1989**, *90*, 1007–23.
(66) Kendall, R. A.; Dunning, T. H., Jr.; Harrison, R. J. *J. Chem. Phys.* **1992**, *96*, 6796–806.
(67) Woon, D. E.; Dunning, T. H., Jr. *J. Chem. Phys.* **1993**, *98*, 1358–71.

(68) Christen, D.; Griffiths, J. H.; Sheridan, J. *Z. Naturforsch.* **1981**, *36a*, 1378.
(69) Peng, C.; Schlegel, H. B. *Israel J. Chem.* **1993**, *33*, 449.
(70) Peng, C.; Ayala, P. Y.; Schlegel, H. B.; Frisch, M. J. *J. Comput. Chem.* **1996**, *17*, 49.
(71) Fermann, J. T.; Auerbach, S. M. *J. Chem. Phys.* **2000**, *112*, 6787–6794.
(72) Nelson, P. H.; Tsapatsis, M.; Auerbach, S. M. *J. Membr. Sci.* **2001**, *184* (2), 245–255.
(73) Iyengar, S. S.; Petersen, M. K.; Burnham, C. J.; Day, T. J. F.; Teige, V. E.; Voth, G. A. *J. Chem. Phys.* **2005**, *123*, 84309.
(74) Iyengar, S. S. *J. Chem. Phys.* **2007**, *126*, 216101.
(75) Iyengar, S. S. *J. Chem. Phys.* **2005**, *123*, 84310.
(76) Bunker, D. L. *Methods Comput. Phys.* **1971**, *10*, 287.
(77) Schlegel, H. B.; Millam, J. M.; Iyengar, S. S.; Voth, G. A.; Scuseria, G. E.; Daniels, A. D.; Frisch, M. J. *J. Chem. Phys.* **2001**, *114*, 9758.
(78) Schlegel, H. B.; Iyengar, S. S.; Li, X.; Millam, J. M.; Voth, G. A.; Scuseria, G. E.; Frisch, M. J. *J. Chem. Phys.* **2002**, *117*, 8694.
(79) Fermann, J. T.; Blanco, C.; Auerbach, S. M. *J. Chem. Phys.* **2000**, *112*, 6779–6786.
(80) Chen, J.; Brooks, C. L.; Scheraga, H. A. *J. Phys. Chem. B* **2008**, *112* (2), 242–249.
(81) McCunn, L. R.; Roscioli, J. R.; Johnson, M. A.; McCoy, A. B. *J. Phys. Chem. B* **2008**, *112*, 321–327.
(82) Nemukhin, A. V.; Grigorenko, B. L.; Topol, I. A.; Burt, S. K. *J. Phys. Chem. B* **2003**, *107*, 2958–2965.
(83) Gettinger, C. L.; Heeger, A. J.; Drake, J. M.; Pine, D. J. *J. Chem. Phys.* **1994**, *101*, 1673–78.
(84) Heffner, G. W.; Pearson, D. S. *Macromolecules* **1991**, *24*, 6295–99.
(85) Mena-Osteritz, E.; Meyer, A.; Langeveld-Voss, B.; Janssen, R.; Meijer, E.; Bäuerle, P. *Angew. Chem.* **2000**, *112*, 2791–96.